

Lattice swelling and modulus change in a helium-implanted tungsten alloy: X-ray micro-diffraction, surface acoustic wave measurements, and multiscale modelling

F. Hofmann,^{a,*} D. Nguyen-Manh,^{b,c} M.R. Gilbert,^{b,c} C.E. Beck,^c J.K. Eliason,^d A.A. Maznev,^d W. Liu,^e D.E.J. Armstrong,^c K.A. Nelson^d and S.L. Dudarev^{b,c}

^aDepartment of Engineering Science, University of Oxford, Parks Road, Oxford OX1 3PJ, UK

^bCCFE, Culham Science Centre, Abingdon OX14 3DB, UK

^cDepartment of Materials, University of Oxford, Parks Road, Oxford OX1 3PH, UK

^dDepartment of Chemistry, Massachusetts Institute of Technology, 77 Massachusetts Avenue, Cambridge, MA 02139, USA

^eAdvanced Photon Source, Argonne National Lab, 9700 South Cass Avenue, Argonne, IL 60439, USA

Received 22 July 2014; revised 21 January 2015; accepted 23 January 2015

Available online 26 February 2015

Abstract—Using X-ray micro-diffraction and surface acoustic wave spectroscopy, we measure lattice swelling and elastic modulus changes in a W-1% Re alloy after implantation with 3110 appm of helium. An observed lattice expansion of a fraction of a per cent gives rise to an order of magnitude larger reduction in the surface acoustic wave velocity. A multiscale model, combining elasticity and density functional theory, is applied to the interpretation of observations. The measured lattice swelling is consistent with the relaxation volume of self-interstitial and helium-filled vacancy defects that dominate the helium-implanted material microstructure. Larger scale atomistic simulations using an empirical potential confirm the findings of the elasticity and density functional theory model for swelling. The reduction of surface acoustic wave velocity predicted by density functional theory calculations agrees remarkably well with experimental observations.

© 2015 Acta Materialia Inc. Published by Elsevier Ltd. All rights reserved.

Keywords: Helium implantation; Micro-diffraction; Elastic properties; Density functional theory; Empirical potential

1. Introduction

Tungsten (W) and tungsten-based alloys are the main candidate materials for plasma facing divertor surfaces in future fusion power plants [1] due to their high melting point, good resistance to sputtering, high thermal conductivity, and low tritium retention rate [2–5]. In addition to the radiation damage produced by collision cascades [6], bombardment of tungsten with 14.1 MeV fusion neutrons also transmutes it into other chemical elements through nuclear reactions. Calculations show that significant amounts of rhenium (Re) (~ 0.2 at.% year^{−1}), tantalum (~ 0.1 at.% year^{−1}) and osmium (~ 0.1 at.% year^{−1}) will be produced during the operation of a DEMO fusion reactor [7]. The amount of helium (He) produced by transmutation in tungsten is relatively small (between 0.1 and 10 appm year^{−1}) [7]. During operation tungsten surfaces in the divertor will also be exposed to large fluxes of hydrogen isotopes and helium ions with a broad spectrum of

energies, resulting in a high heat flux of up to 15 MW/m² [8].

High-flux low-energy helium ion implantation causes significant modifications of the material surface (e.g. formation of sponge-like structures, “fuzz” and bubbles) even at ion energies below the sputtering threshold (~ 100 eV) [9–11]. Similar effects have been observed at intermediate helium ion energies (30 keV) and temperatures from 1000 K to 1400 K [12,13]. At high temperatures it is expected that the implanted helium atoms diffuse deeper into the bulk, affecting material behaviour due to their strong interaction with irradiation defects [14]. For example, it has been found experimentally, by nano-indentation, that the combined effect of helium implantation and cascade damage from self-ion irradiation on hardness is far greater than that of cascade damage alone [15].

An important question concerns the dominant mechanism by which helium is retained in the tungsten matrix. Positron Annihilation Spectroscopy (PAS) studies [16,17] and ab-initio calculations [18] indicate that helium-induced microstructure in metals is driven by the propensity of helium atoms to form bound complexes with vacancies. These may be pre-existing vacancies or vacancies formed

*Corresponding author. +44 1865 283 446.; e-mail: felix.hofmann@eng.ox.ac.uk

by helium agglomeration and self-trapping leading to the spontaneous production of Frenkel pairs [19,20]. Helium also has a significant effect on radiation-induced microstructure through the suppression of vacancy and self-interstitial atom (SIA) recombination since helium atoms rapidly fill vacant lattice sites [21]. At elevated temperatures the resulting availability of excess SIAs stimulates nucleation and growth of interstitial dislocation loops [22].

Due to these complex interactions, carrying out quantitative analysis of the microstructure formed as a result of helium ion implantation proves challenging [23]. The majority of recoil events produced by helium ions during implantation have energy lower than ~ 100 eV (see Fig. 1(c)). Such low energy recoil events produce only individual Frenkel pairs, and hence the microstructure of helium ion irradiated tungsten is expected to be dominated by helium-filled vacancies and vacancy clusters, and SIA defects. The objective of the analysis given below is to correlate experimentally measured strains and elastic properties with the notion of such a damage microstructure through the use of data on defect properties derived from *ab initio* calculations, elasticity theory and larger scale atomistic calculations with an empirical potential.

2. Experimental measurements

2.1. Sample preparation

To mimic transmutation-induced production of rhenium in tungsten, a W-1 at.% Re alloy was manufactured by arc melting from high purity elemental powders [24]. 1 mm thick slices were polished using diamond paste and 50 nm colloidal silica suspension to produce a flat, damage-free surface. Optical micrographs show equiaxed grains with sizes ranging from 100 to 1000 μm (Fig. 1(a)). Electron back scattered diffraction (EBSD) indicated no significant texture.

Helium ions were implanted at 300 °C to a depth of ~ 2.8 μm using a 2 MeV ion accelerator at the National Ion Beam Centre, University of Surrey, UK. To achieve a near uniform helium ion concentration in excess of 3000 appm throughout the implanted layer, implantations

were carried out at 12 different ion-energies and fluences [24]. The resulting implantation profile, predicted by the Stopping and Range of Ions in Matter (SRIM) code [25], assuming a Frenkel pair formation threshold energy of 68 eV [26], is shown in Fig. 1(b). At depths between 1 and 2 μm the calculated implanted helium dose is 3110 ± 270 appm. The associated displacement damage is 0.24 ± 0.02 displacements per atom (dpa). Analysis of recoils caused by the implanted helium ions (Fig. 1(c)) shows that they are predominantly low energy events. Hence we expect mainly the formation of individual Frenkel pairs during implantation, rather than clusters of defects [27]. This is also confirmed by transmission electron microscopy (TEM) of pure tungsten samples implanted with helium under the same conditions, which showed no visible defects after implantation, indicating that all of the implantation-induced defects formed at 300 °C are below the TEM resolution limit [15].

2.2. Micro-diffraction measurements

Lattice swelling due to helium implantation was measured by micro-beam Laue diffraction at beamline 34-ID-E at the Advanced Photon Source, Argonne National Lab, USA. Fig. 2(a) shows a schematic of the experimental setup. The incident, polychromatic (7–30 keV) X-ray beam was focussed by Kirkpatrick-Baez (KB) mirrors to a probe spot with 600 nm vertical and 400 nm horizontal full width at half maximum and near Lorentzian shape. The sample was positioned at the focus in 45° reflection geometry. Diffraction patterns were recorded on a Perkin Elmer flat panel detector mounted in 90° reflection geometry above the sample. The Differential Aperture X-ray Microscopy (DAXM) technique was used to determine the depth in the sample from which different scattered contributions originated [28–30]. For DAXM measurements a 50 μm diameter platinum wire was scanned through the diffracted beams. By triangulating using the wire edge, depth-resolved Laue patterns were reconstructed at 500 nm intervals along the incident beam direction. A detailed description of the experimental setup and analysis routines is provided elsewhere [29,31,32].

Laue diffraction patterns containing more than 20 peaks were collected at 3 positions in the implanted sample. The

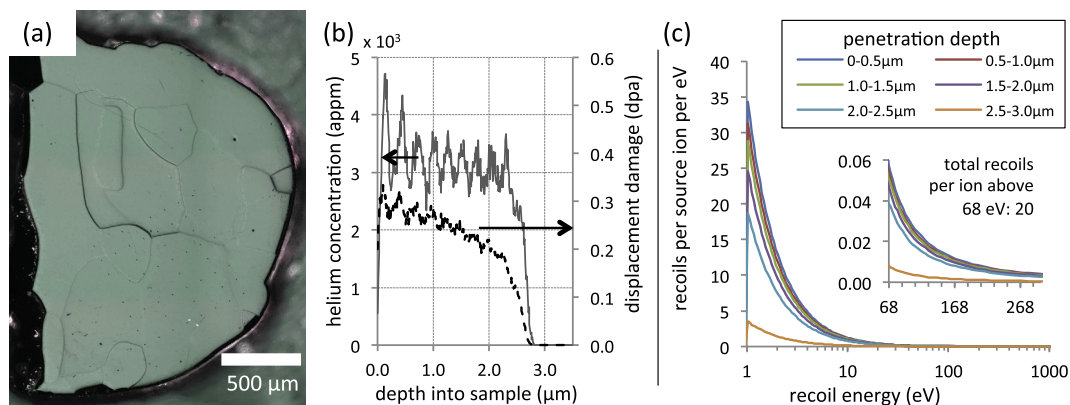


Fig. 1. (a) Representative optical micrograph of the W-1% Re material. (b) SRIM calculated profile of injected helium ion concentration (grey curve) and implantation-induced displacement damage (black curve) as a function of depth in the sample. (c) Primary recoil atom energy spectrum per source ion calculated for different depths in the sample. On average each source ion produces 20 recoils with energy greater than the Frenkel pair formation threshold energy of 68 eV.

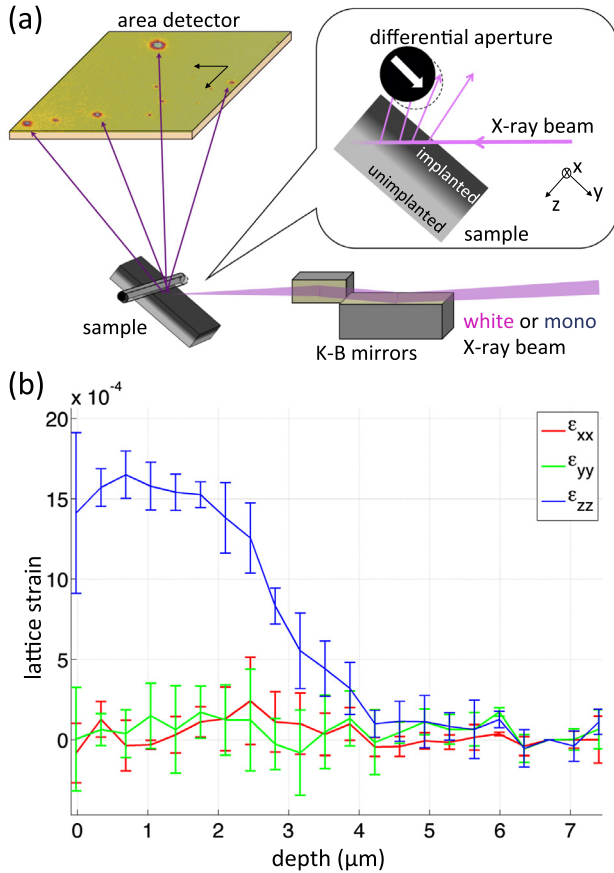


Fig. 2. Laue diffraction measurements: (a) Schematic of the experimental configuration illustrating the orientation of the sample with respect to the incident beam, scanning wire and detector, as well as the orientation of the sample coordinate axes. (b) Experimentally-measured direct elastic strains in sample coordinates. The error-bars indicate the variation associated with experimental measurements.

XMAS (<https://sites.google.com/a/lbl.gov/bl12-3-2/user-resources>) [33] and LaueGo (J.Z. Tischler: tischler@anl.gov) software packages were used to determine the deviatoric lattice strain tensor, ϵ^* , from the Laue patterns. By scanning of the incident X-ray beam energy, using the beamline monochromator ($\Delta E/E \approx 10^{-4}$), the absolute lattice spacing of the (5,1,4) reflection was determined. Combining this with the deviatoric strain tensor, ϵ^* , the full elastic lattice strain tensor, ϵ , was calculated [34–36]. By applying the DAXM technique to both polychromatic and energy resolved scans the depth variation of the total lattice strain tensor, ϵ , was measured. Fig. 2(b) shows the ϵ_{zz} out-of-plane strain component and the ϵ_{xx} and ϵ_{yy} in-plane strain components averaged over three measurement locations. The standard deviation of measured values (shown as error bars in Fig. 2(b)) provides an indication of the experimental variation [31,37,38].

Elastic strains in the unimplanted substrate material, at depths greater than $\sim 4 \mu\text{m}$, are close to zero. The measured lattice constant in that region is $3.1650 \pm 0.0007 \text{ \AA}$, close to the literature value of $3.16522 \pm 0.00009 \text{ \AA}$ for pure tungsten [39]. This provides a built-in validation for our strain measurements and suggests that 1% rhenium alloying does not have a significant effect on the crystallography of the tungsten base.

In the helium-implanted surface layer there is a substantial increase in the ϵ_{zz} out-of-plane strain component, whilst the ϵ_{xx} and ϵ_{yy} in-plane strain components remain close to zero. This suggests out-of-plane swelling of the crystal lattice due to helium implantation and irradiation defects with constraint in the directions parallel to the surface due to the requirement of continuity at the interface between the implanted layer and the substrate. A similar effect has been observed in UO_2 implanted with 60 keV He ions [40]. The depth of $3 \mu\text{m}$ (Fig. 2(b)) up to which the helium-implantation-induced positive (i.e. tensile) ϵ_{zz} strain extends agrees well with the maximum implantation depth of $2.8 \mu\text{m}$ predicted by SRIM. This provides independent experimental validation for the light ion penetration depth predicted by SRIM calculations [25].

At depths between 1 and $2 \mu\text{m}$ the calculated helium implantation profile (Fig. 1(a)) is comparatively flat with an average helium concentration of $3110 \pm 270 \text{ appm}$. The measured average ϵ_{zz} strain for these depths is $(1550 \pm 120) \times 10^{-6}$. Since tungsten is almost perfectly elastically isotropic at room temperature [41–43], linear isotropic elasticity can be used to determine the hydrostatic strain, ϵ_v , due to helium-implantation-induced defects. Assuming a spatially homogeneous distribution of randomly-oriented defects in the implanted layer and given that $\epsilon_{xx} = \epsilon_{yy} = 0$, the ϵ_{zz} lattice strain can be written as (see Appendix for more detail):

$$\epsilon_{zz} = \frac{\epsilon_v}{3} + 2 \frac{\nu}{(1-\nu)} \frac{\epsilon_v}{3}, \quad (1)$$

where ν is the Poisson ratio. The first term in Eq. (1) captures the increase in ϵ_{zz} due to the homogeneous hydrostatic strain, ϵ_v , i.e. lattice swelling. The second term is due to the Poisson effect which arises from the lateral constraint on the implanted layer, i.e. $\epsilon_{xx} = \epsilon_{yy} = 0$. From the measured ϵ_{zz} we estimate $\epsilon_v = 2620 \times 10^{-6} \pm 200 \times 10^{-6}$ (using $\nu = 0.28$ [41–43]).

Stresses in the implanted layer are given by the following expressions, derived in the Appendix:

$$\sigma_{xx} = \sigma_{yy} = \frac{\nu E}{(1+\nu)(1-2\nu)} \epsilon_{zz} = \frac{\nu E}{3(1-\nu)(1-2\nu)} \epsilon_v, \quad (2)$$

$$\sigma_{zz} = \frac{(1-\nu)E}{(1+\nu)(1-2\nu)} \epsilon_{zz} = \frac{E}{3(1-2\nu)} \epsilon_v = K \epsilon_v, \quad (3)$$

where K is the bulk modulus and E the Young modulus. Assuming $\nu = 0.28$ and $E = 410 \text{ GPa}$ [41–43], we find $\sigma_{zz} = 0.81 \pm 0.06 \text{ GPa}$ and $\sigma_{xx} = \sigma_{yy} = 0.32 \pm 0.02 \text{ GPa}$. The σ_{zz} stress component is associated with the density of internal forces exerted on the material by the helium-implantation-induced defects homogeneously distributed in the implanted layer. The in-plane stress components, σ_{xx} and σ_{yy} , are due to the same internal defect-induced forces and the boundary condition requiring the continuity of the material at the interface between the implanted layer and the substrate. Boundary conditions for the elasticity equations describing strains and stresses in the implanted layer and in the substrate are given in the Appendix. We note that the defect-induced stresses in the implanted surface layer represent a significant fraction of the yield stress of the material, which is close to 1 GPa .

The stress contribution, σ_{ii}^{BC} , due to the boundary conditions in our sample is given by:

$$\sigma_{ii}^{BC} = \sigma_{ii} - p^{defect}, \quad (4)$$

where p^{defect} is the hydrostatic stress due to internal defect forces. Note that in Eq. (4) and elsewhere no Einstein summation rule is implied, and σ_{ii} refers to one of the diagonal elements of the stress tensor. Since $\sigma_{zz}^{BC} = 0$ GPa, it follows that $p^{defect} = 0.81 \pm 0.06$ GPa and hence $\sigma_{xx}^{BC} = \sigma_{yy}^{BC} = -0.49 \pm 0.08$ GPa.

2.3. Surface acoustic wave measurements

Measurement of the Rayleigh velocity, c_r , of surface acoustic waves (SAW) provides an accurate means of determining the elastic properties of the helium-implanted layer. We use the laser-induced transient grating (TG) technique to measure the change of c_r between implanted and unimplanted samples. A schematic of the TG setup, described elsewhere in more detail [44], is shown in Fig. 3(a). Two short excitation pulses (515 nm wavelength, 60 ps pulse duration and 1.75 μ J pulse energy) are crossed on the sample. Interference of the two pulses results in a spatially sinusoidal excitation pattern, which, when absorbed, causes rapid thermal expansion and generation of two counter-propagating SAWs. The SAW wavelength, λ , is determined by the period of the interference pattern. Here a nominal value of $\lambda = 2.75$ μ m was chosen to ensure that the SAW

signal in the helium-implanted sample is dominated by the ~ 2.8 μ m thick implanted surface layer [45].

Detection of the SAW is achieved by diffraction of a quasi-continuous wave probe beam (532 nm wavelength and 10 mW average power) from the induced sample surface displacement and refractive index variations. The diffracted beam is collinear with a reflected reference beam to achieve heterodyne detection (Fig. 3(a)). The combined beam is sent to a fast avalanche photo-diode (2 GHz bandwidth) and time traces are recorded with an oscilloscope. The excitation spot measured 500 μ m diameter at 1/e intensity level and the probe spot 300 μ m.

The recorded probe signal for the unimplanted W-1% Re sample (Fig. 3(b)) shows a non-exponentially decaying background, due to the decaying temperature grating [46], on which oscillations, due to the surface acoustic waves, are superimposed. By taking the Fourier transform of the time trace (inset in Fig. 3(b)) the frequency of the Rayleigh waves, f , can be determined. An approximate solution for the Rayleigh wave speed, c_r , in an elastically isotropic medium is given by [47]:

$$c_r = f\lambda \approx (0.874 + 0.196\nu - 0.043\nu^2 - 0.055\nu^3) \sqrt{\frac{E}{2(1+\nu)\rho}}, \quad (5)$$

where ρ is the mass density (19260 kg m⁻³ for the samples used here [41–43]). The integral error of this approximate solution over the range $\nu \in [-1, 0.5]$ is 0.20% [48], which is sufficiently accurate for the relative comparisons performed here.

For the unimplanted W-1% Re sample we measured $c_r = 2680 \pm 2$ ms⁻¹ and for the helium-implanted sample $c_r = 2621 \pm 7$ ms⁻¹, i.e. c_r is reduced by 2.2%. The SAW measurements averaged over several grains in the sample and no significant grain-to-grain variation of c_r was found, suggesting that tungsten remains close to being isotropically elastic after helium implantation. In a W-1% Ta alloy implanted to the same helium dose under the same conditions a similar reduction of c_r by 1.6% was observed.

3. Calculations

To elucidate the mechanisms that lead to the experimentally observed lattice swelling and Rayleigh wave velocity reduction, we combined Density Functional Theory (DFT), larger scale atomistic simulations using an empirical potential and elasticity calculations.

DFT calculations were performed using the Perdew–Burke–Ernzerhof electron exchange–correlation functional within generalized gradient approximation (PBE-GGA). We used the projector augmented wave (PAW) pseudopotentials implemented in the Vienna Ab-initio Simulation Package (VASP) [49,50]. Given that semicore electronic states make a non-negligible contribution to the formation energies of self-interstitial atom (SIA) defects [51], all the calculations were performed using the PAW potentials Xpv , where the semicore p states are treated as valence states. In all the cases considered here a $4 \times 4 \times 4$ bcc supercell, with plane wave cut-off energy of 400 eV, and a $4 \times 4 \times 4$ k -point mesh with spacing of 0.15 \AA^{-1} were used. Helium-induced defects, such as interstitial helium-clusters, helium-vacancy clusters and $\langle 111 \rangle$ SIA defects were

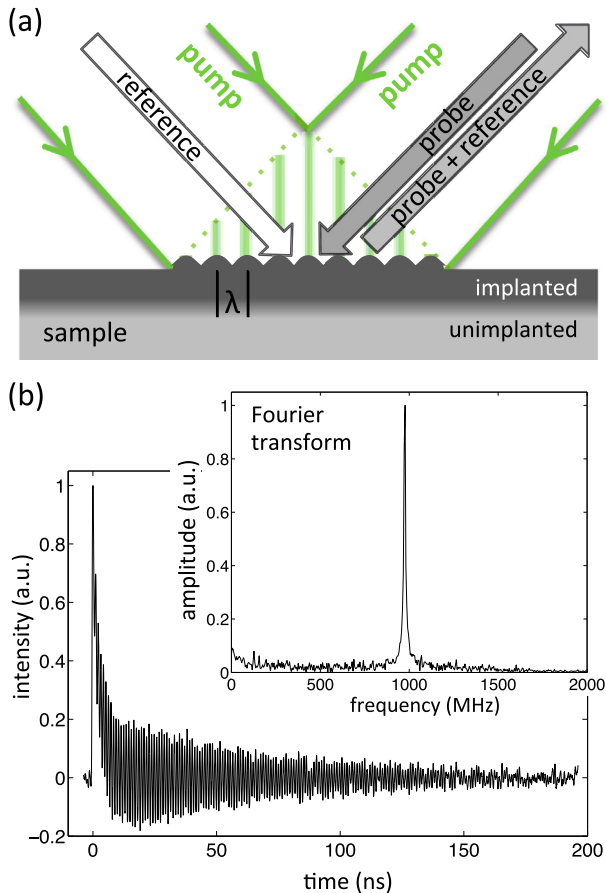


Fig. 3. Transient grating surface acoustic wave measurements: (a) Schematic of the experimental setup. (b) Measured intensity signal plotted as a function of delay time relative to the pump pulse for the unimplanted W-1% Re sample. Fourier transform of the signal showing a peak at the surface acoustic wave frequency (inset).

introduced into the cell. The system was then fully relaxed, with unconstrained, periodic boundary conditions. The broadening scheme of Methfessel–Paxton (MP) [52], which leads to reasonable results for relaxation in metallic systems, was used with a broadening width of 0.1 eV. Calculations for body-centred cubic (bcc) tungsten with a Gaussian broadening scheme and a 2 atom cell yielded very similar results to those obtained using the MP scheme (e.g. elastic constants: Gaussian scheme: $C_{11} = 518.7$, $C_{12} = 199.9$ and $C_{44} = 141.9$; MP scheme: $C_{11} = 517.4$, $C_{12} = 199.3$ and $C_{44} = 142.2$ (in GPa)).

Larger-scale atomistic calculations were carried out using the most recent empirical interatomic potential for bcc tungsten [53]. Self-interstitial atom defects, which dominate swelling in the material (this conclusion is also supported by DFT calculations, see the DFT section below), were introduced with random orientation and spatial distribution in an otherwise perfect bcc box containing 65,536 atoms ($32 \times 32 \times 32$ bcc unit cells in the normal Cartesian coordinate system). To reproduce the lateral constraint matching that of experiments, the size of the simulation box was fixed in two directions ($x = [100]$ and $y = [010]$). Unconstrained expansion was only allowed in the third direction ($z = [001]$). Molecular relaxation was then performed assuming periodic boundary conditions in all directions.

4. Results and discussion

4.1. Formation and relaxation volumes of defects

Relating the observed macroscopic strains in the helium-implanted layer to the microscopic characteristics of individual defects requires evaluation of the elastic dipole tensor of defects P_{ij} [54], also known as the double-force tensor [55]. In cubic crystals the trace of a defect dipole tensor is proportional to the product of the bulk modulus, K , and the relaxation volume of the defect, Ω_r [56]:

$$\text{Tr}P_{ij} = 3 K \Omega_r. \quad (6)$$

Using DFT, we calculate Ω_r for a number of helium-implantation-induced defects. Alternatively P_{ij} could be obtained directly from constant supercell volume calculations [57,58]. Ω_r is defined as the volume change associated with the introduction of a defect in a simulation cell, i.e.:

$$\Omega_r = \Omega(\text{defect}) - \Omega(\text{perfect}). \quad (7)$$

Here $\Omega(\text{perfect})$ is the volume initially occupied by the perfect, defect free, $4 \times 4 \times 4$ supercell, whereas $\Omega(\text{defect})$ is the volume occupied by the same, relaxed, supercell containing a defect. Relaxation volume provides a measure of elastic strain in the vicinity of the defect [59]. It also enters the elasticity equations for the stress and strain fields resulting from the accumulation of defects, as described in the Appendix.

Table 1 lists Ω_r values calculated for a number of helium-implantation-induced defects. Table 1(a) shows that Ω_r of vacancies and vacancy clusters is negative, whilst Ω_r for SIAs is large and positive. The relaxation volume of a Frenkel pair, $\Omega_r(\text{Frenkel})$, is given by the sum $\Omega_r(\text{Frenkel}) = \Omega_r(\text{V}) + \Omega_r(\text{SIA}) = 1.31 \Omega_0$. This means that $\Omega_r(\text{Frenkel})$ is positive and greater than Ω_0 , the perfect atomic volume (15.85 \AA^3 in tungsten at 298 K [39]). Relaxation volumes for interstitial He_n clusters (Table 1(b)) are all positive and, to a good approximation, increase linearly with n for $1 \leq n \leq 5$. The calculated relaxation volumes for vacancy defects and interstitial helium defects are in good agreement with values reported by other authors [60–62]. For He_nV defects (Table 1(c)) the relaxation volume changes sign from negative to positive as the number of helium atoms increases. For a He_2V defect the relaxation volume is close to zero.

4.2. Lattice strain and swelling

Using the relaxation volumes of defects derived from DFT it is now possible to compute the lattice strain associated with the accumulation of helium and implantation-induced defects in the implanted surface layer. It is essential to distinguish between two possible modes of swelling: One is associated with the accumulation of vacancies in the bulk of the material and migration of self-interstitial atoms to the surface. This (Shottky) swelling mode does explain the increase of volume of the sample, but predicts very low elastic strain. Moreover, since the relaxation volume of vacancy defects is negative, the lattice strain associated with this mode of swelling is expected to be compressive (negative). This is not observed in our experiments. The alternative (Frenkel) model assumes that both self-interstitial and vacancy defects are retained in the implanted layer, and that the observed strains and stresses result from

Table 1. Relaxation volumes, Ω_r , of various defects in pure tungsten. Values are calculated by DFT and are given in atomic volume units Ω_0 . (a) Relaxation volumes of vacancies and self-interstitials (V: vacancy, V_2 : di-vacancy, V_3 : tri-vacancy, SIA: self-interstitial atom). (b) Relaxation volumes of interstitial He_n clusters. (c) Relaxation volumes of He_nV clusters.

(a) Relaxation volumes of vacancies and self-interstitial atom defects					
V	V_2 (1NN)	V_2 (2NN)	V_2 (3NN)	V_3 (1NN(2) + 2NN)	<111> SIA
−0.37	−0.72	−0.79	−0.76	−1.08	1.68
−0.34 [60]	−0.65 [60]	−0.74 [60]	−0.69 [60]		
−0.38 [61]					
(b) Relaxation volumes of interstitial helium clusters					
He (tetra)	He (octa)	He_2 (tetra)	He_3 (tetra)	He_4 (tetra)	He_5 (tetra)
0.36	0.37	0.80	1.16	1.65	2.03
0.33 [62]	0.34 [62]				
(c) Relaxation volumes of helium – vacancy clusters					
HeV (tetra)	HeV (octa)	He_2V (tetra)	He_3V (tetra)	He_4V (tetra)	He_5V (tetra)
−0.24	−0.23	−0.06	0.14	0.38	0.71
					1.09

the forces exerted by the defects on the surrounding material. The experimental X-ray diffraction data suggest that it is the Frenkel model for defect accumulation and lattice swelling that describes our implantation experiments.

To evaluate lattice swelling associated with defects accumulated in the implanted layer, we consider the density of forces exerted on the material by the defects [54]:

$$F_i(\mathbf{r}) = -\sum_{\alpha} P_{i\alpha}^{(\alpha)} \frac{\partial}{\partial x_i} \delta(\mathbf{r} - \mathbf{R}_{\alpha}), \quad (8)$$

where \mathbf{R}_{α} is the coordinate of a defect and \mathbf{r} the coordinate vector. The stress tensor can now be evaluated by considering the equilibrium condition [54]:

$$\frac{\partial}{\partial x_j} \sigma_{ij} + F_i(\mathbf{r}) = 0. \quad (9)$$

If an implanted volume is free of constraints in all directions, averaging over the distribution of defects and random orientations of defects gives:

$$\sigma_{ii} = p^{defect} = \frac{1}{3} \sum_A n^{(A)} \text{Tr} P_{ij}^{(A)}, \quad (10)$$

where summation is performed over defect types, A , each with number density $n^{(A)}$, and σ_{ii} is as described by Eq. (4) for the case of $\sigma_{ii}^{BC} = 0$. Using Eq. (6), we arrive at the following expression for defect-induced lattice swelling:

$$\varepsilon_v = \sum_A n^{(A)} \Omega_r^{(A)}. \quad (11)$$

This equation is one of the central results of this paper (see Appendix for a detailed mathematical treatment). It relates the macroscopic lattice swelling to the average concentrations of defects and their relaxation volumes. Combining it with Eq. (1), we arrive at an expression for the out-of-plane lattice strain, ε_{zz} , that is expected for a given defect population in an implanted layer subject to the lateral constraints present in our sample:

$$\varepsilon_{zz} = \frac{1}{3} \frac{(1+v)}{(1-v)} \sum_A n^{(A)} \Omega_r^{(A)}. \quad (12)$$

Using this equation, we can now quantitatively study the type of microstructure formed as a result of helium implantation. *Ab-initio* studies point out that helium has a strong affinity to vacancies [18]. Hence we first assume that each implanted helium atom occupies a vacancy, preventing recombination of some of the vacancies and SIAs formed during implantation. All Frenkel defects that are not filled with helium are assumed to recombine. This is reasonable since recoils produced during the ion-implantation are predominantly low energy events (Fig. 1(c)). SRIM calculations [25] indicate that the mean energy of primary knock on atoms (PKAs) with energy greater than the tungsten displacement threshold (68 eV) is 340 eV. At this energy the predicted mean implantation depth is ~ 6 Å, i.e. 2 unit cells, making recombination likely. Post neutron irradiation studies of high-temperature recovery in tungsten also indicate that at the implantation temperature of 300 °C recombination of the majority of the generated Frenkel pairs is expected [63].

Using Eq. (12) and the relaxation volumes given in Table 1, the strain due to a homogeneous distribution of 3110 appm of HeV defects and the corresponding 3110 appm of SIAs can be evaluated. Such an “evenly

balanced” assumed microstructure is characterised by an average strain $\varepsilon_{zz} = 2654 \times 10^{-6}$. This is almost twice the level of strain observed experimentally.

Helium clustering offers an explanation for the lower experimentally observed ε_{zz} strain. According to our DFT calculations, which agree with the analysis performed earlier [20,64], vacancies can be readily occupied by several helium atoms. This reduces the concentration of $\langle 111 \rangle$ SIA defects and the strain in the implanted layer. If we assume that all the vacancies are occupied by two helium atoms (i.e. that the defect population consists of 1555 appm He₂V and 1555 appm SIAs), we predict the out of plane elastic strain $\varepsilon_{zz} = 1493 \times 10^{-6}$. This agrees reasonably well with the measured out of plane strain of $\varepsilon_{zz} = 1550 \times 10^{-6}$.

In experiments we measure elastic strain, an integral quantity to which the entire population of helium and radiation-induced defects contributes. Because of this we cannot be more precise in our assessment of the defect microstructure formed by the helium implantation. However we are able to conclude that helium implantation in tungsten at 300 °C results in helium-filled vacancies, which, on average, contain more than one helium atom per vacancy. Furthermore, as detailed below, we find that the observed lattice swelling is almost entirely due to the accumulation of self-interstitial atom defects, characterised by large relaxation volumes, which cause lattice expansion.

Two key assumptions in our defect analysis are: first that the orientations of the defects are random; and second that swelling scales linearly with defect concentration, which is the case in the low defect concentration limit. To validate these assumptions we performed a series of larger-scale atomistic simulations using an empirical potential to describe interactions between tungsten atoms. From DFT calculations we found that the measured lattice swelling is consistent with a defect structure dominated by He₂V clusters and SIAs. The relaxation volumes of a He₂V cluster and a $\langle 111 \rangle$ SIAs are $-0.06 \Omega_0$ and $1.68 \Omega_0$, respectively (Table 1). This means that He₂V clusters contribute little to lattice volume change. Lattice swelling is instead predominantly due to SIAs. Thus in the atomistic simulations only SIAs were taken into account. The effective SIA concentration was varied from 1000 to 4000 appm, and for each case 10 random SIA configurations were relaxed. Fig. 4(a) and (b), respectively show the calculated out of plane strain (ε_{zz}) and the in-plane residual stresses ($\sigma_{xx}^{BC} = \sigma_{yy}^{BC}$, due to the lateral constraints ($\varepsilon_{xx} = \varepsilon_{yy} = 0$), as functions of SIA concentration. Both quantities show a linear dependence on concentration, confirming the appropriateness of the low concentration limit assumption. For an SIA concentration of 1555 appm the predicted out of plane strain, ε_{zz} , is 1240×10^{-6} compared to a measured value of 1550×10^{-6} . The magnitude of the predicted in-plane residual stresses, due to the zero lateral strain boundary conditions, $\sigma_{xx}^{BC} = \sigma_{yy}^{BC}$ are -0.39 GPa, somewhat lower than the value of -0.49 GPa determined from experiments. Thus it appears that atomistic simulations using the most up to date empirical potential for tungsten [53] underestimate the helium-implantation-induced stresses and strains by 20%. Still, this is a reasonable agreement given the absence of parameters associated with these kinds of deformations from the database used to fit the interatomic potential.

Fig. 4(c) shows a relaxed configuration for an SIA concentration of 1602 appm, corresponding to 105 SIAs in the simulation box. Delocalisation of SIAs into crowdions is

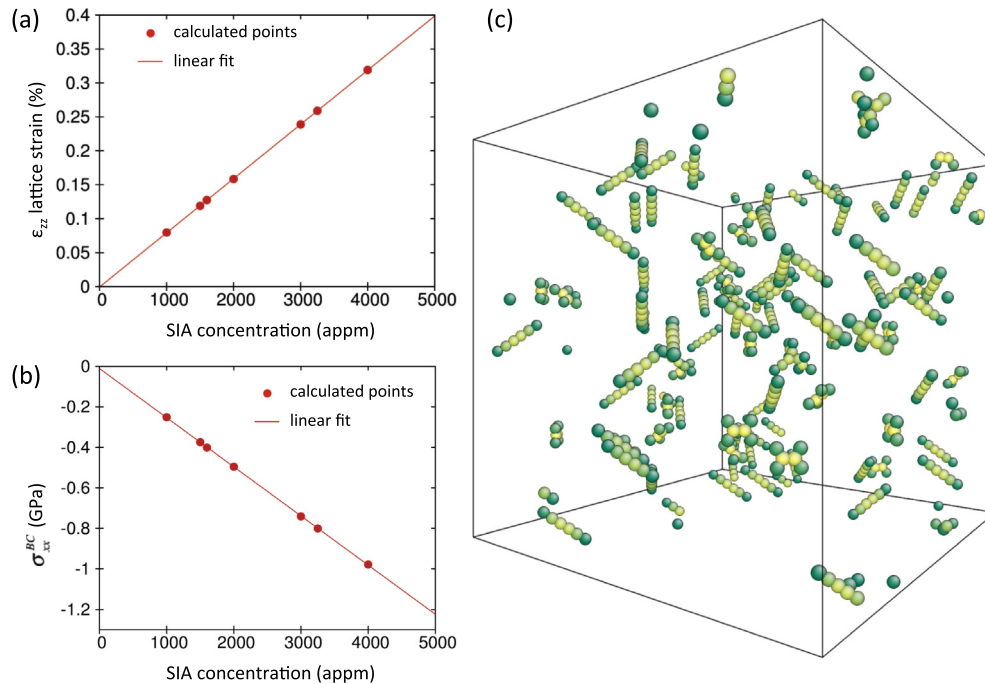


Fig. 4. Lattice swelling and stresses due to SIAs calculated by larger scale atomistic simulations using an empirical potential: (a) Calculated ε_{zz} lattice strain as a function of SIA concentration. (b) σ_{xx}^{BC} stress, due to lateral boundary conditions, as a function of SIA concentration. (c) Relaxed configuration snapshot of a larger scale atomistic calculation with 105 SIA defects (1602 appm SIA concentration).

clearly visible [65]. They are aligned along a number of different $\langle 111 \rangle$ directions, justifying the assumption of a randomly oriented defect population.

An interesting question concerns the effect of defect clustering on the validity of our analysis. At the implantation temperature of 300 °C, vacancies in tungsten are not mobile [51,66,67]. Thus no significant clustering of vacancies, whether filled with helium or not, is expected. SIAs in tungsten on the other hand form delocalised $\langle 111 \rangle$ crowdions that are highly mobile even at room temperature [51]. In pure tungsten samples, implanted with helium under the same conditions, no significant clustering of SIAs, leading to the formation of interstitial prismatic dislocation loops, was observed in TEM micrographs [15]. However, there may still be small self-interstitial defect clusters present that are below the TEM resolution limit (i.e. containing fewer than ~ 60 SIAs). Fig. 5 shows a plot of relaxation volume for SIA clusters containing N SIAs, plotted as a function of N . Here, atomic relaxations were performed, using the same empirical potential used earlier, on circular discs of SIAs inserted into a perfect bcc lattice containing between a few hundred thousand and a few million atoms. In the limit of large disc size ($N = 1000$), the relaxed defect structure was the expected prismatic $\frac{1}{2}\langle 111 \rangle$ dislocation loop, whilst at smaller sizes (below $N \sim 100$) the defect remained more like a platelet of crowdions. Since no visible defects were observed in TEM [15], Fig. 5 concentrates on SIA clusters with $N < 100$. For such clusters the cluster relaxation volume appears to scale approximately linearly with N . Thus the swelling analysis presented above is still valid, even if some small SIA clusters below the TEM resolution limit exist. In the limit of large N ($\gg 100$) the relaxation volume, treated as a function of the number of self-interstitial atoms, tends asymptotically to $\Omega_r = N\Omega_0$, where Ω_0 is the atomic volume.

Specific to the present sample is the role played by rhenium, which is a trap for SIAs (0.95 eV binding energy) [68]. Both rhenium atoms and helium-filled vacancies act as obstacles to SIA motion, reducing clustering and preventing SIA escape to sinks, such as the sample surface or grain boundaries. The mobility of interstitial helium is not affected by the presence of rhenium (0.01 eV binding energy) [69].

The good match between predicted lattice swelling and experiments confirms our assumption that the vast majority of helium-implantation-generated Frenkel defects recombine. Only a small proportion is being prevented from doing so by the injected helium. According to our SRIM calculations, each implanted helium ion generates on

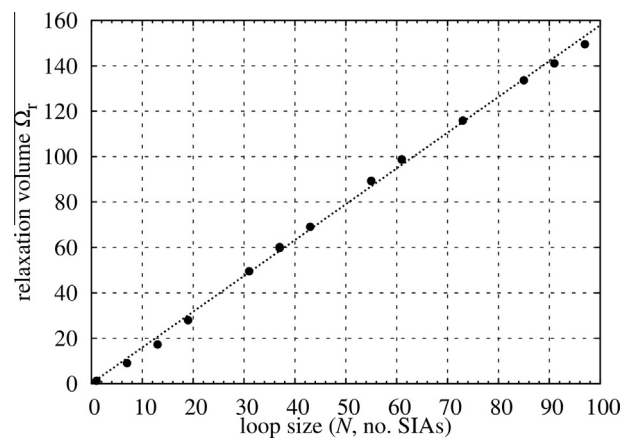


Fig. 5. Relaxation volume for SIA loops containing N SIAs, plotted as a function of N . Values are calculated by large scale atomistic simulations using an empirical potential and are given in atomic volume units Ω_0 . The straight line fit to the data has a slope of 25.4 \AA^3 .

Table 2. (a) Elastic parameters of perfect tungsten and tungsten containing SIA and He₂V defects calculated by DFT and rescaled. (b) Calculated elastic constants for helium-implanted tungsten (W + 1555 appm He₂V + 1555 appm SIAs). (c) Isotropic elastic constants and SAW velocities for pure tungsten and helium-implanted tungsten. Values calculated based on rescaled elastic constants are highlighted in grey.

(a) Elastic properties calculated by DFT					
		C ₁₁ (GPa)	C ₁₂ (GPa)	C ₄₄ (GPa)	A
Pure W, experiment at 298 K [41–43]		522.8	203.5	160.7	1.01
Pure W	From DFT	537.4	188.2	153.7	0.88
	Rescaled	522.8	203.5	160.7	1.01
W + SIA	From DFT	512.5	212.5	141.4	0.94
	Rescaled	498.6	229.8	147.8	1.10
W + He ₂ V	From DFT	518.9	188.1	141.2	0.85
	Rescaled	504.8	203.4	147.6	0.98

(b) Calculated elastic constants for the helium-implanted layer					
		C ₁₁ (GPa)	C ₁₂ (GPa)	C ₄₄ (GPa)	A
Helium-implanted W	From DFT	528.8	193.0	148.8	0.89
	Rescaled	514.4	208.7	155.5	1.02

(c) Isotropic elastic constants (calculated using Voigt) and surface acoustic wave velocity						
		K (GPa)	G (GPa)	E (GPa)	ν	c _r (ms ^{−1})
Pure W	From DFT	304.6	162.1	413.0	0.274	2679
	Rescaled	309.9	160.3	410.1	0.279	2666
Helium-implanted W	From DFT	304.9	156.4	400.7	0.281	2634
	Rescaled	310.6	154.5	397.5	0.287	2621

average ~ 74 Frenkel pairs (see Fig. 1(b) and (c)). Of these, only 0.5 Frenkel pairs persist. This means that less than 1% of the calculated dpa is actually retained in the material, making the value of using dpa as a measure of the “actual” irradiation-induced damage questionable.

4.3. Surface acoustic wave velocity reduction

To elucidate the decrease in the surface acoustic wave velocity resulting from helium implantation, the changes in elastic properties that arise due to He₂V clusters and $\langle 111 \rangle$ SIAs were evaluated using DFT. A detailed description of the method used to calculate elastic constants is given elsewhere [68,70–72].

The fully relaxed $4 \times 4 \times 4$ DFT supercell for perfect bcc tungsten exhibits the expected O_h symmetry. The calculated elastic constants C_{11} , C_{12} and C_{44} are listed in

Table 2(a). When an SIA is introduced into the simulation cell, a $[111]$ crowdion is formed [51] (see relaxed configuration shown in Fig. 6(a)). The relaxed $4 \times 4 \times 4$ supercell containing one SIA exhibits a significant distortion and the resulting loss of symmetry. The supercell now has D_{3d} symmetry, retaining 3 reflection and 3 rotation symmetries of the total of 48 symmetries of the original defect-free structure. This means that 8 distinct defect orientations exist. To obtain the elastic constants of a $4 \times 4 \times 4$ supercell containing a randomly orientated SIA defect the stiffness tensor calculated by DFT was averaged over all 8 possible configurations. The resulting elastic constants are listed in Table 2(a).

For the He₂V cluster, a vacancy was introduced in the centre of the $4 \times 4 \times 4$ supercell and two helium atoms were placed in the tetrahedral positions at opposite sides of the vacancy. Fig. 6(b) shows the He₂V cluster after

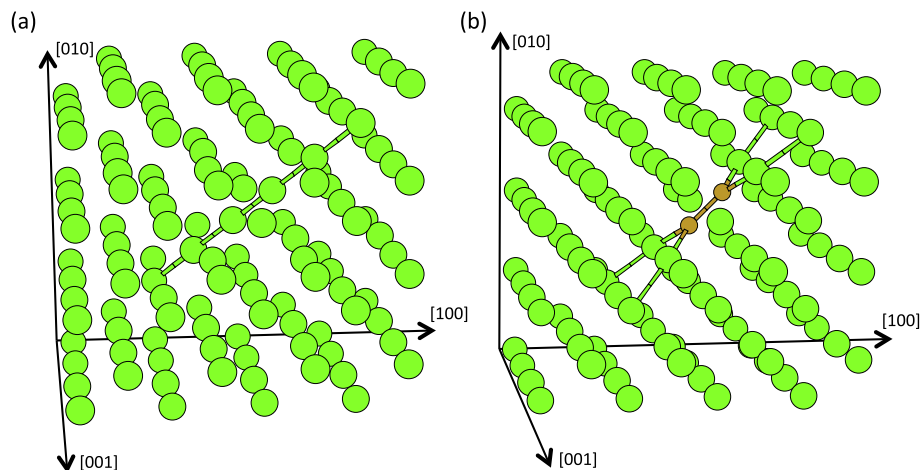


Fig. 6. Relaxed defect configurations from DFT for: (a) $[111]$ SIA. (b) He₂V cluster.

relaxation. The two helium atoms align along the [110] direction and form a defect in the $(\bar{1}10)$ plane. The resulting supercell has C_{1h} symmetry, retaining only one, reflection, symmetry element. Hence there are 24 distinct defect orientations. The elastic constants, found for the $4 \times 4 \times 4$ supercell when averaging over these configurations, are listed in Table 2(a).

The elastic constants calculated by DFT for defect-free tungsten in a $4 \times 4 \times 4$ supercell (Table 2(a)) correspond to the anisotropy factor $A = 2C_{44}/(C_{11} - C_{12}) = 0.88$.

Experimentally measured elastic constants of tungsten show a decrease of A from $A = 1.01$ at room temperature ($T = 298$ K) [41–43] to $A = 0.98$ at $T = 4.2$ K [73], whilst also indicating that tungsten is close to being elastically isotropic. The DFT value for the anisotropy factor, calculated at $T = 0$ K, reproduces the experimental trend of $A < 1$ at low temperature, but its value deviates from the experimentally measured one. There are two main factors that explain this difference: The first is that elastic constants were evaluated at the DFT equilibrium volume. This is often slightly different from the experimental one; the difference depends on the choice of exchange-correlation functional. The second is the sensitivity of the computed elastic constants to k-space sampling. We also performed DFT calculations for the cases of perfect tungsten with 2 atoms per bcc cubic cell and 1 atom per bcc primitive cell. The smaller cell size allowed for a finer k-space sampling. The calculated values of A were 0.89 and 0.93, for 2 atoms and 1 atom respectively, closer to experimental observations. Including s-electron semi core states in the calculations did not have a significant effect on the predicted elastic constants. Indeed using the PAW potential in the VASP library for the semi core s-electrons yielded an anisotropy factor of 0.88.

To correct for the difference between experiments and DFT calculations we introduce rescaling factors f_{11} , f_{12} and f_{44} , defined as $f_{ij} = C_{ij}^{\text{exp}}(\text{pure W})/C_{ij}^{\text{DFT}}(\text{no defect})$. Here $C_{ij}^{\text{exp}}(\text{pure W})$ are the experimentally measured constants for pure tungsten at room temperature (Table 2(a)) and $C_{ij}^{\text{DFT}}(\text{no defect})$ are the constants calculated from DFT for the defect-free $4 \times 4 \times 4$ tungsten supercell. Treating the changes to elastic constants that arise due to He_2V and SIA defects as small perturbations, the same rescaling factors were applied to the elastic constants calculated by DFT for a supercell containing He_2V or SIA defects, i.e.:

$$C_{ij}^{\text{DFT rescaled}}(\text{defect}) = f_{ij} C_{ij}^{\text{DFT}}(\text{defect}). \quad (13)$$

The resulting values for elastic constants are listed in Table 2(a). The elastic constants for the helium-implanted material were then calculated using the Voigt approach [74]:

$$C_{ij}^{\text{implanted}} = (1 - 128(n^{\text{SIA}} + n^{\text{He}_2\text{V}}))C_{ij}^{\text{W}} + 128n^{\text{SIA}}C_{ij}^{\text{SIA}} + 128n^{\text{He}_2\text{V}}C_{ij}^{\text{He}_2\text{V}}, \quad (14)$$

where n are the number densities of SIA and He_2V defects (1555 appm), and the factor of 128 accounts for the number of atoms contained within the DFT supercell for which elastic constants were computed. The resulting elastic constants for the helium-implanted layer are given in Table 2(b).

For helium-implanted tungsten A remains close to 1, such that it may be reasonably approximated by isotropic elasticity. The bulk modulus, K , and shear modulus, G , are given by [74]:

$$K = \frac{1}{3}(C_{11} + 2C_{12}), \quad (15)$$

$$G = \frac{1}{5}(C_{11} - C_{12} + 3C_{44}). \quad (16)$$

Using isotropic elasticity relations, it is then a straightforward matter to calculate the Young modulus, E , and the Poisson ratio, ν :

$$E = \frac{9KG}{1 + 3\frac{K}{G}}, \quad \nu = \frac{(K - \frac{2}{3}G)}{2(K + \frac{2}{3}G)}. \quad (17)$$

Using Eq. (5) we evaluate the Rayleigh wave velocity, c_r . For unimplanted tungsten we find $c_r = 2666 \text{ ms}^{-1}$, in good agreement with the experimental value of $2680 \pm 2 \text{ ms}^{-1}$. The predicted decrease of the Rayleigh velocity following helium-implantation is 1.7%, compared to the experimentally measured decrease of 2.2%. This agreement is remarkable since, other than the scaling factors of Eq. (13), which in any case do not influence the ratios of the relevant elastic constants, there are no adjustable parameters in our model. Furthermore we note that this reduction can only be achieved by considering both the SIA and He_2V cluster contributions. Separately, SIAs and He_2V clusters would only yield reductions of 1.0% and 0.7% respectively.

Similar calculations were also carried out using the Reuss approach [75]. The calculated c_r values for pure tungsten and helium-implanted tungsten are 2666 ms^{-1} and 2617 ms^{-1} , respectively, indicating a reduction of 1.8%. This is very similar to the value calculated using the Voigt approach, as expected, given that the material remains nearly elastically isotropic after implantation.

We also evaluated the elastic constants predicted by atomistic calculations with the same empirical potential used for the lattice swelling analysis, but this time without the lateral constraint during relaxation, which is consistent with the DFT calculations. The resulting constants are listed in Table 3(a) for defect free tungsten and a $32 \times 32 \times 32$ unit cell simulation box containing 102 randomly oriented SIAs

Table 3. (a) Elastic properties of defect-free tungsten and tungsten containing 1556 appm SIAs calculated using larger scale atomistic simulations with an empirical interatomic potential. (b) Isotropic elastic constants and surface acoustic wave velocities computed for defect free tungsten and tungsten containing 1556 appm SIAs.

<i>(a) Elastic constants calculated by MD using the Marinica et al. potential [53]</i>					
	C_{11} (GPa)	C_{12} (GPa)	C_{44} (GPa)	A	
Pure W	523	202	161	1.00	
W + 1555 appm SIAs	528.8	208.7	168.0	1.05	
<i>(b) Isotropic elastic constants (calculated using Voigt) and surface acoustic wave velocities</i>					
	K (GPa)	G (GPa)	E (GPa)	ν	c_r (ms ^{−1})
Pure W	309.0	160.8	411.1	0.278	2670
W + 1555 appm SIAs	315.4	164.8	421.1	0.278	2703

(i.e. 1556 appm SIA concentration). The Voigt isotropic elastic constants were then calculated using Eqs. (15)–(17) and the surface acoustic wave velocities estimated using Eq. (5) (Table 3(b)). We note that the atomistic calculations predict an *increase* of surface acoustic wave velocity by 1.2% due to SIAs. This is not in agreement with either our DFT calculations, or the experimental measurements. The most probable reason for the disagreement is that the empirical interatomic potential is not able to correctly describe the variation of elastic constants as a function of strain, a point that is fairly difficult to include in the existing potential fitting methodology [53].

5. Conclusions

In this paper we have demonstrated the feasibility of using synchrotron X-ray micro-beam diffraction to quantify lattice swelling in a few micron-thick helium-implanted tungsten layer. Using elasticity theory and relaxation volumes calculated by DFT for various helium-induced defects, we explained the experimentally measured swelling. Agreement between calculations and experiments is good, confirming that small helium-vacancy clusters and SIAs dominate the helium-implantation-induced microstructure. Larger scale atomistic calculations that use an empirical inter-atomic potential and consider the effect of SIAs alone agreed well with the experimentally observed swelling, indicating that lattice swelling is indeed dominated by the presence of SIAs. Surface acoustic wave measurements, using the transient grating technique, showed a decrease of Rayleigh velocity in the helium-implanted material. Using a model based on DFT and elasticity theory, we interpret the reduction in Rayleigh wave velocity, in good agreement with experiments.

Acknowledgements

We thank B. Abbey, A. De Backer and S. G. Roberts for helpful comments and stimulating discussions, as well as A. Xu and G. Hughes for help with sample preparation. FH acknowledges funding from the John Fell fund (122/643) and the Royal Society (RG130308). DNM acknowledges the International Fusion Energy Research Centre (IFERC) for use of the supercomputer (Helios) at the Computational Simulation Centre (CSC) in Rokkasho (Japan). DEJA acknowledges the Royal Academy of Engineering for support through a Research Fellowship. The SAW measurements at MIT were supported by NSF Grant No. CHE-1111557. Use of the Advanced Photon Source, an Office of Science User Facility operated for the U.S. Department of Energy (DOE) Office of Science by Argonne National Laboratory, was supported by the U.S. DOE under contract No. DE-AC02-06CH11357. In part this work has been carried out within the framework of the EUROfusion Consortium and has received funding from the Euratom Research and Training Programme 2014–2018 under grant agreement No. 633053. To obtain further information on the data and models underlying this paper please contact PublicationsManager@ccfe.ac.uk. The views and opinions expressed herein do not necessarily reflect those of the European Commission. This work was part-funded by the United Kingdom Engineering and Physical Sciences Research Council via programme grants EP/G050031 and EP/H018921.

Appendix A.

In this Appendix we give an elastic solution to the problem of ion-induced swelling, relating microscopic

parameters of radiation defects to the macroscopic strains and stresses developing in the material due to the accumulation of defects during ion implantation.

A defect in an isotropic elastic medium (tungsten is elastically isotropic) generates a field of atomic displacements of the form [54],

$$u_i^{(x)} = -P_{ks}^{(x)} \frac{\partial}{\partial x_s} G_{ik}(\mathbf{r} - \mathbf{R}_x), \quad (\text{A1})$$

where \mathbf{R}_x is the position vector of a defect and $P_{ks}^{(x)}$ is the defect's dipole tensor, corresponding to the density of forces of the form $f_k(\mathbf{r}) = -P_{ks}^{(x)} \frac{\partial}{\partial x_s} \delta(\mathbf{r})$. For an ensemble of defects the density of forces is given by the sum over all the defects in the material

$$F_k(\mathbf{r}) = -\sum_x P_{ks}^{(x)} \frac{\partial}{\partial x_s} \delta(\mathbf{r} - \mathbf{R}_x). \quad (\text{A2})$$

The elastic stress tensor satisfies the equilibrium condition [76]:

$$\frac{\partial}{\partial x_j} \sigma_{ij} + F_i(\mathbf{r}) = 0, \quad (\text{A3})$$

and is related to the elastic strain tensor ε_{ij} through the equation [76]:

$$\sigma_{ij} = \frac{E}{1+\nu} \left(\varepsilon_{ij} + \frac{\nu}{1-2\nu} \varepsilon_{ll} \delta_{ij} \right). \quad (\text{A4})$$

We are interested in evaluating the density of forces resulting from defects homogeneously distributed in a certain element of volume of the material (in our case, the implanted layer). Averaging over the spatial distribution of defects in the implanted volume, we find

$$\begin{aligned} F_k(\mathbf{r}) &= -\sum_x P_{ks}^{(x)} \frac{\partial}{\partial x_s} \int \delta(\mathbf{r} - \mathbf{R}_x) \frac{d\mathbf{R}_x}{V} \\ &= -\sum_x P_{ks}^{(x)} \frac{1}{V} \frac{\partial}{\partial x_s} \Theta(\mathbf{r}) \\ &= -\sum_A \frac{N^{(A)}}{V} P_{ks}^{(A)} \frac{\partial}{\partial x_s} \Theta(\mathbf{r}), \end{aligned} \quad (\text{A5})$$

where function $\Theta(\mathbf{r})$ is equal to unity inside the element of volume occupied by the randomly distributed defects, and vanishes outside this volume element. Elastic stress and strain fields generated by the randomly distributed radiation defects can be described by a suitably chosen density of forces acting *at the interfaces* between the regions containing defects, and regions free of defects. For a planar implanted layer such interfaces are the surface of the material and the internal interface between the implanted layer and the underlying substrate. We assume that the sample occupies the half-space $z > 0$.

The density of forces now has the form:

$$F_k(\mathbf{r}) = -\sum_A n^{(A)} P_{ks}^{(A)} \frac{\partial}{\partial x_s} \Theta(z), \quad (\text{A6})$$

where $\Theta(z) = 1$ for $0 < z < L$, where L is the thickness of the implanted layer, and $n^{(A)}$ is the volume density of defects of type A . Integrating the above equation, we obtain,

$$F_k(\mathbf{r}) = F_k(z) = -\sum_A n^{(A)} P_{ks}^{(A)} (\delta(z) - \delta(z - L)), \quad (\text{A7})$$

The accumulation of anisotropic defects in the implanted layer could give rise to non-vanishing x, y components of force in the plane of the surface. In the absence of direct experimental evidence for such forces, we only consider the z -component of the density of forces:

$$\begin{aligned} F_z(\mathbf{r}) &= F_z(z) = -\sum_A n^{(A)} P_{zz}^{(A)} (\delta(z) - \delta(z-L)) \\ &= -\frac{1}{3} \sum_A n^{(A)} \text{Tr}(P_{ij}^{(A)}) (\delta(z) - \delta(z-L)). \end{aligned} \quad (\text{A8})$$

The use of trace of defect dipole tensor stems from the fact that defects adopt random orientations in the implanted layer. The formula can be simplified if we note [56] that $\text{Tr}(P_{ij}^{(A)}) = \frac{E}{1-2\nu} \Omega_r^{(A)}$, where $\Omega_r^{(A)}$ is the relaxation volume of a defect of type A .

The elastic equilibrium conditions have the form [76]:

$$\frac{\partial}{\partial z} \sigma_{zz} + F_z(z) = 0; \quad \frac{\partial}{\partial z} \sigma_{xz} = \frac{\partial}{\partial z} \sigma_{yz} = 0. \quad (\text{A9})$$

At the free surface $z = 0$ we supplement them with the traction-free boundary conditions $\sigma_{xz}(z = 0) = \sigma_{yz}(z = 0) = \sigma_{zz}(z = 0) = 0$ and find,

$$\frac{\partial}{\partial z} \sigma_{zz} = \frac{1}{3} \sum_A n^{(A)} \text{Tr}(P_{ij}^{(A)}) (\delta(z) - \delta(z-L)), \quad (\text{A10})$$

$$\sigma_{zz} = \frac{1}{3} \sum_A n^{(A)} \text{Tr}(P_{ij}^{(A)}) (\Theta(z) - \Theta(z-L)). \quad (\text{A11})$$

Stresses are concentrated entirely within the implanted layer. The substrate extending from $z = L$ to $z = \infty$ is unaffected by the implantation-induced defects.

Elastic strain tensor is related to the stress tensor through [76]:

$$\varepsilon_{ij} = \frac{1}{E} ((1+\nu)\sigma_{ij} - \nu\sigma_{kk}\delta_{ij}). \quad (\text{A12})$$

From this equation, taking into account that $\varepsilon_{xx} = \varepsilon_{yy} = 0$, we find

$$\varepsilon_{zz} = \frac{(1+\nu)(1-2\nu)}{E(1-\nu)} \sigma_{zz}, \quad (\text{A13})$$

and

$$\varepsilon_{zz} = \frac{(1+\nu)}{3(1-\nu)} \sum_A n^{(A)} \Omega_r^{(A)} (\Theta(z) - \Theta(z-L)). \quad (\text{A14})$$

This formula gives the magnitude of swelling resulting from the accumulation of defects in the implanted layer.

We can also evaluate the two in-plane components of the stress tensor:

$$\sigma_{xx} = \sigma_{yy} = \frac{Ev}{3(1-\nu)(1-2\nu)} \sum_A n^{(A)} \Omega_r^{(A)} (\Theta(z) - \Theta(z-L)). \quad (\text{A15})$$

The component of the stress tensor normal to the surface is,

$$\sigma_{zz} = \frac{E}{3(1-2\nu)} \sum_A n^{(A)} \Omega_r^{(A)} (\Theta(z) - \Theta(z-L)). \quad (\text{A16})$$

The off-diagonal components of the stress tensor vanish both in the implanted layer and in the substrate, namely $\sigma_{xy} = \sigma_{yz} = \sigma_{zx} = 0$ for $0 < z < \infty$.

References

- [1] H. Bolt, V. Barabash, W. Krauss, J. Linke, R. Neu, S. Suzuki, N. Yoshida, A.U. Team, *J. Nucl. Mater.* 329–333 (2004), Part A:66.
- [2] M. Rieth, S.L. Dudarev, S.M. Gonzalez de Vicente, J. Aktaa, T. Ahlgren, S. Antusch, D.E.J. Armstrong, M. Balden, N. Baluc, M.F. Barthe, W.W. Basuki, M. Battabyal, C.S. Becquart, D. Blagoeva, H. Boldyryeva, J. Brinkmann, M. Celino, L. Ciupinski, J.B. Correia, A. De Backer, C. Domain, E. Gaganidze, C. García-Rosales, J. Gibson, M.R. Gilbert, S. Giusepponi, B. Gludovatz, H. Greuner, K. Heinola, T. Höschel, A. Hoffmann, N. Holstein, F. Koch, W. Krauss, H. Li, S. Lindig, J. Linke, C. Linsmeier, P. López-Ruiz, H. Maier, J. Matejcek, T.P. Mishra, M. Muhammed, A. Muñoz, M. Muzyk, K. Nordlund, D. Nguyen-Manh, J. Opschoor, N. Ordás, T. Palacios, G. Pintsuk, R. Pippan, J. Reiser, J. Riesch, S.G. Roberts, L. Romaner, M. Rosiński, M. Sanchez, W. Schulmeyer, H. Traxler, A. Ureña, J.G. van der Laan, L. Veleva, S. Wahlberg, M. Walter, T. Weber, T. Weitkamp, S. Wurster, M.A. Yar, J.H. You, A. Zivelonghi, *J. Nucl. Mater.*, 432 (2013), 482.
- [3] M. Rieth, J.L. Boutard, S.L. Dudarev, T. Ahlgren, S. Antusch, N. Baluc, M.F. Barthe, C.S. Becquart, L. Ciupinski, J.B. Correia, C. Domain, J. Fikar, E. Fortuna, C.C. Fu, E. Gaganidze, T.L. Galán, C. García-Rosales, B. Gludovatz, H. Greuner, K. Heinola, N. Holstein, N. Juslin, F. Koch, W. Krauss, K.J. Kurzydowski, J. Linke, C. Linsmeier, N. Luzginova, H. Maier, M.S. Martínez, J.M. Missaen, M. Muhammed, A. Muñoz, M. Muzyk, K. Nordlund, D. Nguyen-Manh, P. Norajitra, J. Opschoor, G. Pintsuk, R. Pippan, G. Ritz, L. Romaner, D. Rupp, R. Schäublin, J. Schlosser, I. Uytendhouwen, J.G. van der Laan, L. Veleva, L. Ventelon, S. Wahlberg, F. Willaime, S. Wurster, M.A. Yar, *J. Nucl. Mater.* 417 (2011) 463.
- [4] P. Norajitra, L.V. Boccaccini, A. Gervash, R. Giniyatulin, N. Holstein, T. Ihli, G. Janeschitz, W. Krauss, R. Kruessmann, V. Kuznetsov, A. Makhankov, I. Mazul, A. Moeslang, I. Ovchinnikov, M. Rieth, B. Zeep, *J. Nucl. Mater.* 367–370 (2007), Part B:1416.
- [5] A.C. Rion, J.V. Thomas, *Phys. Scr.* 2001 (2001) 9.
- [6] A.E. Sand, S.L. Dudarev, K. Nordlund, *Europhys. Lett.* 103 (2013) 46003.
- [7] M.R. Gilbert, S.L. Dudarev, S. Zheng, L.W. Packer, J.-C. Sublet, *Nucl. Fusion* 52 (2012) 083019.
- [8] D. Maisonnier, D. Campbell, I. Cook, L.D. Pace, L. Giancarli, J. Hayward, A.L. Puma, M. Medrano, P. Norajitra, M. Rocella, P. Sardain, M.Q. Tran, D. Ward, *Nucl. Fusion* 47 (2007) 1524.
- [9] M.J. Baldwin, R.P. Doerner, *Nucl. Fusion* 48 (2008) 035001.
- [10] K. Shin, S. Wataru, O. Noriyasu, Y. Naoaki, S. Tsubasa, *Nucl. Fusion* 49 (2009) 095005.
- [11] Y. Zayachuk, M.H.J.t. Hoen, P.A.Z.v. Emmichoven, D. Terentyev, I. Uytendhouwen, G.v. Oost, *Nucl. Fusion* 53 (2013) 013013.
- [12] S. Sharafat, A. Takahashi, K. Nagasawa, N. Ghoniem, J. Nucl. Mater. 389 (2009) 203.
- [13] S.J. Zenobia, L.M. Garrison, G.L. Kulcinski, *J. Nucl. Mater.* 425 (2012) 83.
- [14] N. Yoshida, *J. Nucl. Mater.* 266–269 (1999) 197.
- [15] D.E.J. Armstrong, P.D. Edmondson, S.G. Roberts, *Appl. Phys. Lett.* 102 (2013) 1.
- [16] A. Debele, M.F. Barthe, T. Sauvage, R. Belamhawal, A. Chelgoum, P. Desgardin, H. Labrim, J. Nucl. Mater. 362 (2007) 181.

- [17] P.E. Lhuillier, T. Belhabib, P. Desgardin, B. Courtois, T. Sauvage, M.F. Barthe, A.L. Thomann, P. Brault, Y. Tessier, *J. Nucl. Mater.* 416 (2011) 13.
- [18] C.-C. Fu, F. Willaime, *Phys. Rev. B* 72 (2005) 064117.
- [19] W.D. Wilson, C.L. Bisson, M.I. Baskes, *Phys. Rev. B* 24 (1981) 5616.
- [20] J. Boisse, C. Domain, C.S. Becquart, *J. Nucl. Mater.* 455 (2014) 10.
- [21] G. Lucas, R. Schaublin, *J. Phys.: Condens. Matter* 20 (2008) 415206.
- [22] S. Moll, T. Jourdan, H. Lefaix-Jeuland, *Phys. Rev. Lett.* 111 (2013) 015503.
- [23] J. Marian, T.L. Hoang, *J. Nucl. Mater.* 429 (2012) 293.
- [24] C.E. Beck, S.G. Roberts, P.D. Edmondson, D.E.J. Armstrong, *MRS Online Proc. Library* 1514 (2013) 99.
- [25] J.F. Ziegler, M.D. Ziegler, J.P. Biersack, *Nucl. Instrum. Methods Phys. Res. B: Beam Interact. Mater. Atoms* 268 (2010) 1818.
- [26] A. International, E521 Standard Practice for Neutron Radiation Damage Simulation by Charged-Particle Irradiation, ASTM International, West Conshohocken, PA, 2009.
- [27] P. Erhart, J. Marian, *J. Nucl. Mater.* 414 (2011) 426.
- [28] B.C. Larson, W. Yang, G.E. Ice, J.D. Budai, J.Z. Tischler, *Nature* 415 (2002) 887.
- [29] W. Liu, G. Ice, B. Larson, W. Yang, J. Tischler, J. Budai, *Metall. Mater. Trans. A* 35 (2004) 1963.
- [30] W. Yang, B.C. Larson, J.Z. Tischler, G.E. Ice, J.D. Budai, W. Liu, *Micron* 35 (2004) 431.
- [31] F. Hofmann, B. Abbey, W. Liu, R. Xu, B.F. Usher, E. Balaur, Y. Liu, *Nat. Commun.* (2013) 4.
- [32] W. Liu, P. Zschack, J. Tischler, G. Ice, B. Larson, *AIP Conf. Proc.* 1365 (2011) 108.
- [33] N. Tamura, R.S. Celestre, A.A. MacDowell, H.A. Padmore, R. Spolenak, B.C. Valek, N.M. Chang, A. Manceau, J.R. Patel, Submicron X-ray diffraction and its applications to problems in materials and environmental science, Papers from the 12th National Synchrotron Radiation Instrumentation Conference, vol. 73, AIP, Madison, Wisconsin (USA), 2002, p. 1369.
- [34] J.-S. Chung, G.E. Ice, *J. Appl. Phys.* 86 (1999) 5249.
- [35] O. Robach, J.-S. Micha, O. Ulrich, P. Gergaud, *J. Appl. Crystallogr.* 44 (2011) 688.
- [36] O. Robach, J.-S. Micha, O. Ulrich, O. Geaymond, O. Sicardy, J. Hartwig, F. Rieutord, *Acta Crystallogr. A* 69 (2013) 164.
- [37] F. Hofmann, S. Eve, J. Belnoue, J.-S. Micha, A.M. Korsunsky, *Nucl. Instrum. Methods Phys. Res. A: Accelerators Spectrometers, Detectors Assoc. Equipment* 660 (2011) 130.
- [38] J. Petit, M. Bornert, F. Hofmann, O. Robach, J.-S. Micha, O. Ulrich, C. Le Boulrot, D. Faurie, A.M. Korsunsky, O. Castelnau, *Proc. IUTAM* 4 (2012) 133.
- [39] W. Parrish, *Acta Crystallogr. A* 13 (1960) 838.
- [40] A. Richard, H. Palancher, E. Castelier, J.-S. Micha, M. Gamaleri, G. Carlot, H. Rouquette, P. Goudeau, G. Martin, F. Rieutord, J.P. Piron, P. Garcia, *J. Appl. Crystallogr.* 45 (2012) 826.
- [41] D.I. Bolef, J. De Klerk, *J. Appl. Phys.* 33 (1962) 2311.
- [42] F.H. Featherston, J.R. Neighbours, *Phys. Rev.* 130 (1963) 1324.
- [43] R. Lowrie, A.M. Gonas, *J. Appl. Phys.* 38 (1967) 4505.
- [44] J.A. Johnson, Optical characterization of complex mechanical and thermal transport properties. Department of Chemistry, vol. PhD, Cambridge, MA: Massachusetts Institute of Technology, 2011.
- [45] J. Goossens, P. Leclaire, X. Xu, C. Glorieux, L. Martinez, A. Sola, C. Siligardi, V. Cannillo, T. VanderDonck, J.-P. Celis, *J. Appl. Phys.* (2007) 102.
- [46] O.W. Käding, H. Skurk, A.A. Maznev, E. Matthias, *Appl. Phys. A* 61 (1995) 253.
- [47] G.M. Peter, *Nanotechnology* 16 (2005) 995.
- [48] M. Rahman, T. Michelitsch, *Wave Motion* 43 (2006) 272.
- [49] G. Kresse, J. Furthmüller, *Phys. Rev. B* 54 (1996) 11169.
- [50] G. Kresse, J. Hafner, *Phys. Rev. B* 47 (1993) 558.
- [51] D. Nguyen-Manh, A.P. Horsfield, S.L. Dudarev, *Phys. Rev. B* 73 (2006) 020101.
- [52] M. Methfessel, A.T. Paxton, *Phys. Rev. B* 40 (1989) 3616.
- [53] M.C. Marinica, V. Lisa, M.R. Gilbert, L. Proville, S.L. Dudarev, J. Marian, G. Bencteux, F. Willaime, *J. Phys.: Condens. Matter* 25 (2013) 395502.
- [54] G. Leibfried, N. Breuer, *Point Defects in Metals I: Introduction to the Theory*, Springer-Verlag, Berlin, 1978.
- [55] H. Trinkaus, *Phys. Status Solidi (b)* 51 (1972) 307.
- [56] P. Ehrhart, *J. Nucl. Mater.* 69–70 (1978) 200.
- [57] C. Varvenne, F. Bruneval, M.-C. Marinica, E. Clouet, *Phys. Rev. B* 88 (2013) 134102.
- [58] R.G.A. Veiga, M. Perez, C.S. Becquart, E. Clouet, C. Domain, *Acta Mater.* 59 (2011) 6963.
- [59] A.M. Kosevich, *The Crystal Lattice: Phonons, Solitons, Dislocations*, Wiley-VCH Verlag, Berlin, 2005.
- [60] D. Kato, H. Iwakiri, K. Morishita, *J. Nucl. Mater.* 417 (2011) 1115.
- [61] K. Heinola, T. Ahlgren, K. Nordlund, J. Keinonen, *Phys. Rev. B* 82 (2010) 094102.
- [62] H.B. Zhou, S. Jin, X.L. Shu, Y. Zhang, G.H. Lu, F. Liu, *Europhys. Lett.* 96 (2011) 66001.
- [63] L.K. Keys, J.P. Smith, J. Moteff, *Phys. Rev.* 176 (1968) 851.
- [64] A. De Backer, P.E. Lhuillier, C.S. Becquart, M.F. Barthe, *J. Nucl. Mater.* 429 (2012) 78.
- [65] P.M. Derlet, D. Nguyen-Manh, S.L. Dudarev, *Phys. Rev. B* 76 (2007) 054107.
- [66] K.D. Rasch, R.W. Siegel, H. Schultz, *Philos. Mag. A* 41 (1980) 91.
- [67] A. Debelle, M.F. Barthe, T. Sauvage, *J. Nucl. Mater.* 376 (2008) 216.
- [68] M. Muzyk, D. Nguyen-Manh, K.J. Kurzydłowski, N.L. Baluc, S.L. Dudarev, *Phys. Rev. B* 84 (2011) 104115.
- [69] W. Xuebang, K. Xiang-Shan, Y. Yu-Wei, C.S. Liu, Q.F. Fang, C. Jun-Ling, G.N. Luo, W. Zhiguang, *Nucl. Fusion* 53 (2013) 073049.
- [70] D. Nguyen-Manh, M. Muzyk, K.J. Kurzydłowski, N.L. Baluc, M. Rieth, S.L. Dudarev, *Key Eng. Mater.* 465 (2011) 15.
- [71] M. Muzyk, D. Nguyen-Manh, J. Wróbel, K.J. Kurzydłowski, N.L. Baluc, S.L. Dudarev, *J. Nucl. Mater.* 442 (2013) S680.
- [72] D. Nguyen-Manh, M.Y. Lavrentiev, M. Muzyk, S.L. Dudarev, *J. Mater. Sci.* 47 (2012) 7385.
- [73] C.E. Anderson, F.R. Brotzen, *J. Appl. Phys.* 53 (1982) 292.
- [74] W. Voigt, *Ann. Phys.* 274 (1889) 573.
- [75] A. Reuss, *ZAMM – J. Appl. Math. Mech./Zeitschrift für Angewandte Mathematik und Mechanik* 9 (1929) 49.
- [76] L.D. Landau, E.M. Lifshitz, *Theory of Elasticity*, Pergamon Press, Oxford, 1970.